Self-recoverable mechanically induced instant luminescence from Cr^{3+}-doped $LiGa_5O_8$

Puxian Xiong, Bolong Huang, Dengfeng Peng, Bruno Viana, Mingying Peng* and Zhijun Ma**

P. Xiong, Prof. M. Peng

School of Physics and Optoelectronic, The State Key Laboratory of Luminescent Materials and Devices, and Guangdong Provincial Key Laboratory of Fiber Laser Materials and Applied Techniques South China University of Technology, Guangzhou 510640, China.

Email: pengmingying@scut.edu.cn

Prof. B. Huang

Department of Applied Biology and Chemical Technology, The Hong Kong Polytechnic University, Hong Hum, Kowloon, Hong Kong SAR, 999077 China

Email: bhuang@polyu.edu.hk

Prof. D. Peng

College of Physics and Optoelectronic Engineering, Shenzhen University, Shenzhen 518060, China

Prof. B. Viana

PSL Research University Chimie ParisTech, IRCP, CNRS, Paris 75005, France

Prof. M. Peng, Prof. Z. Ma

The China-Germany Research Center for Photonic Materials and Device, The State Key Laboratory of Luminescent Materials and Devices, and Guangdong Provincial Key Laboratory of Fiber Laser Materials and Applied Techniques, The School of Materials Science and Engineering, South China University of Technology, Guangzhou 510641, China.

Email: pengmingying@scut.edu.cn, zhijma@scut.edu.cn

Keywords: self-recoverable mechanoluminescence, biostress visualization, trivalent Cr, $LiGa_5O_8$

Currently, most of the mechanoluminescence (ML) phosphors strongly depend on post-irradiation stimulation using ultraviolet light (denoted as "UV exposure" from hereon) to show the ML. However, only a few transition metal cations have been proven to be effective luminescence centers, which hinder the development of more ML phosphors. This work is the first to report a self-recoverable deep-red-to-near-infrared ML using Cr^{3+}-doped $LiGa_5O_8$ phosphor with fully recoverable ML performance. The ML performance can be further optimized by tuning the trap redistributions by codoping the phosphor with Al^{3+} and Cr^{3+} cations. Theoretical calculations revealed the important role of Cr dopants in the modulation of local electronic environments for achieving the ML. Owing to the induced interelectronic levels and shallow electron trap distributions, the electron recombination efficiency is enhanced both through direct tunneling and energy transfer toward the dopant levels. Moreover, the ML of Cr^{3+}-doped $LiGa_5O_8$ can penetrate a 2-mm-thick pork slice, showing that it can have wide-ranging *in vivo* applications, including the optical imaging of intracorporal stress/strain distribution and dynamics. Therefore, this work fabricates a novel ML material with self-recoverable luminescence in an extended wavelength range, which increases the number of potential ML candidates and helps promote the fundamental understanding and practical applications of ML materials.

Mechanoluminescence (ML) involves the emission of photons by materials in response to mechanical stimuli such as compression, fracture, grinding, and stretching.[1-6] Owing to the instantaneous and *in situ* characteristics of ML, ML materials have great potential in various fields such as mechanical sensing,[7] magnetic-optics coupling,[8] visualized sensing,[9] dynamic

pressure mapping,[10] and organic piezo-display devices.[2, 11] In particular, they can be used for *in situ*, real-time, and multidimensional stress/strain mechanical sensing.[11-15] Generally, to improve the ML performance, most ML materials require UV exposure stimulation by high-energy ultraviolet (UV) light to generate charge carriers. This is because once the "prestored" charges are released from their traps in ML materials for light emission, these materials must be irradiated again for further use. For some applications, ML materials need to be coated on the surface of the target object for easy and direct pre-irradiation after each load cycle.[16] However, this strategy does not work in applications that need ML materials to be buried inside other materials. Owing to the shallow tissue-penetration depth and possible tissue damage caused by high-energy UV light, the current ML materials have limited *in vivo* biomedical applications. Thus, it is necessary to develop novel ML materials with self-recoverable emissions and tissue penetration.

To date, many ML materials have been reported, wherein piezoelectric hosts such as $LiNbO_3$, (Ca/Ba)OZnS, and ZnS play a dominant role.[17-22] Generally, the concentration and distribution of traps are critical for determining the ML performance.[23-26] ML materials can be divided into two categories: phosphors that require UV stimulation (non-self-recoverable) and those that do not need such stimulation for ML (self-recoverable). At present, self-recoverable ML has only been reported in the Mn^{2+}/Cu^{+}-doped ZnS phosphor. In 2013, Jeong et al. reported that a ZnS:Cu^{2+} polymer composite film demonstrated ML with a reproducible intensity for over 100,000 cycles of repeated stretching.[27] In 2015, Wang et al. reported that a composite film comprising dispersed ZnS:Mn^{2+} phosphor showed stable ML intensity for over 10,000 cycles of repeated compression tests.[10] They attributed the recoverability of intense ML to the fact that both stretching and releasing processes can induce a local electrical

field that excites electrons in ZnS:Mn^{2+} to realize efficient ML.[10] However, no consensus has been reached on the underlying mechanism for the self-recoverable ML phenomenon.[27] Kim et al. found that the triboelectricity-induced luminescence is more likely to contribute to the mechanically driven luminescence in ZnS.[28] Zhu et al. fabricated a composite containing ZnS:Cu/poly(methyl methacrylate) as a luminescent layer. They also confirmed that ZnS-type phosphors present mechanically induced electroluminescence.[9] Hence, doped ZnS can be considered as a piezoelectricity-induced electroluminescent material. However, this model cannot explain the ML properties of materials such as $SrAl_2O_4$:Eu^{2+} by weak mechanical stimuli, because a weak piezoelectric field cannot impact and excite Eu^{2+}. Other researchers have proposed the piezoelectricity-induced detrapping model to explain the origin of ML.[2, 17] Although this model has been applied to many ML phosphors, no self-recoverable ML phosphor based on such a model has yet been reported.[29] In addition, the emission centers of the existing ML phosphors are usually based on lanthanide cations such as Nd^{3+}, Sm^{3+}, Tm^{3+}, and Pr^{3+}.[30-32] To the best of our knowledge, except for Cu^{+} and Mn^{2+}, other transition metal cations have rarely been shown to behave as ML emission centers.

Compared to Mn^{2+}/Cu^{+}-doped ZnS phosphors, Cr^{3+}-activated deep-red persistent luminescence gallate ($LiGa_5O_8$, for instance) materials have drawn much attention and have also shown potential applications in bioimaging.[33, 34] However, the ML from Cr^{3+} ions has never been reported. Here, for the first time, we report a self-recoverable (that does not need UV light stimulation) deep-red-to-near-infrared ML in Cr^{3+}-doped $LiGa_5O_8$ phosphor. Cr^{3+} is substituted into the 6-coordinated Ga^{3+} site (and stabilized in the octahedral gallium sites) to further generate ML peaking at 716 nm from its $^2E \rightarrow {}^4A_2$ spin-forbidden transition.[35, 36] Because we found that deeper traps (>1.06 eV) may be important for ML, we further

enhanced the trap distribution by codoping with Al^{3+} ions. Moreover, the recovery of ML can be achieved after each cycle without any new light excitation. Hence, we proposed a possible mechanism based on mechanically induced trap recharging to explain the origin of self-recoverable ML in Cr^{3+}-doped $LiGa_5O_8$. DFT calculations revealed the formation of a local piezoelectrical field induced by the incorporation of Cr in the $LiGa_5O_8$ host, which enhances the electronic transfer and promotes the energy conversion. In addition, we demonstrate that ML can deeply penetrate the animal soft tissue and hence it has potential biomedical applications.

Results and discussion

Crystalline structure and micromorphology of $LiGa_5O_8:Cr^{3+}$

The XRD patterns of $LiGa_{5(1-x)}O_8:5xCr^{3+}$ (x = 0.04%, 0.08%, 0.12%, 0.16%, 0.20%, and 0.24%) are depicted in **Figure 1a**. Compared to the reference spectrum of $LiGa_5O_8$, cubic $LiGa_5O_8$ (PDF 38-1371) dominates the crystalline phase in all the doped samples. This result means that all the Cr^{3+} ions are well incorporated into the $LiGa_5O_8$ lattice. To determine the actual crystalline structure of the obtained samples, Rietveld refinement was performed on the sample with x = 0.04%, as presented in Figure 1b. The refinement starts with the powder diffraction data of $LiGa_5O_8$ from PDF 38-1371 and converges with R_p = 7.27%, R_{wp} = 10.4%, R_{exp} = 7.06%, and goodness-of-fit Chi^2 = 2.17 for the XRD data of sample x = 0.04%. A comparison of the experimental and calculated results also confirms that the crystal phase of the sample belongs to the expected cubic noncentrosymmetric $P4_332$ (No. 212) space group.

The refinement results show that $LiGa_5O_8$ has one type of Li site and two types of Ga and O sites. The refinement process produces lattice parameter a = 8.20349 Å and lattice volume V = 552.073 $Å^3$ for the sample with x = 0.04%, which are comparable to a = 8.203 Å and V = 551.970 $Å^3$ of the undoped $LiGa_5O_8$ sample. The crystal structure of $LiGa_5O_8$ is presented in Figure 1c, from which the lattice site occupancy of Cr^{3+} can be determined. Each unit cell consists of three basic structural units: [$Ga1O_6$] octahedral, [LiO_6] octahedral, and [$Ga2O_4$] tetrahedral. For the octahedral unit, the Ga1-O1, Ga1-O2, and Li1-O2 bonds have the same length of 2.05075 Å, and Ga1 and Li1 ions have the same coordination number of 6. For the tetrahedral unit, Ga2 sites are 4-fold coordinated (CN = 4) with a Ga2-O2 bond length of 1.77600 Å. Generally, Cr^{3+} ions cannot stably exist in a tetrahedral site because of the low unstable crystal field, and hence, they prefer to occupy octahedral sites.[37] Therefore, Cr^{3+} cannot occupy the $Ga2^{3+}$ sites here. Clearly, Cr^{3+} (r = 0.615 Å, CN = 6) is preferred to substitute the $Ga1^{3+}$ ions (r = 0.62 Å, CN = 6) than the Li^+ ions (r = 0.76 Å, CN = 6) considering the match in ion radii and valences. To confirm this, the percentage of ion radii between the doping center (Cr^{3+}) and the to-be-substituted ions (Li^+ or Ga^{3+}) was determined: Dr = [|R_m(CN) - R_d(CN)|]/R_m(CN), where R_m and R_d are the Shannon ionic radii of the host and doped ions, respectively. The calculated Dr value of Li^+ was 19.08%, which was much higher than that of $Ga1^{3+}$ (0.81 %). Therefore, Cr^{3+} ions tend to replace $Ga1^{3+}$ ions. The SEM image (upper panel in Figure 1d) reveals irregular columnar particles with an average size of approximately 2 μm. The EDS spectrum (bottom panel in Figure 1d) confirms the existence of Ga, O, and Cr. The absence of Li peaks is attributed to the inability of Li to generate a reliable X-ray signal for detection.[38] Meanwhile, the unlabeled peaks originating from the Au element sputtered on the sample surface to improve conductivity for SEM measurements.

ML properties of $LiGa_5O_8:Cr^{3+}$

ML was observed in Cr^{3+}-activated $LiGa_{5(1-x)}O_8:5xCr^{3+}$ phosphors. The ML band centered at ~716 nm forms due to the $^2E \rightarrow {}^4A_2$ spin-forbidden transition of Cr^{3+} from the 6-fold coordinated site.[39] First, we analyzed the ML spectra of Cr^{3+}-doped samples (**Figure 2a**). When x is 0.04%, the ML signal is too small to be recorded. The ML intensity gradually increased when the concentration of Cr^{3+} doping is increased until x = 0.12%. A further increase in Cr^{3+} doping decreased the ML, confirming that the strongest ML intensity is achieved at x = 0.12%. Subsequently, the ML-intensity dependence of sample x = 0.12% on various loadings was studied, and the related ML spectra are shown in Figure 2b. As the loading was increased from 1000 to 3500 N, the ML intensities continuously increased, demonstrating a linear correlation between the ML intensity and the load. The high linear fitting R^2 = 0.9949 (Figure 2c) indicates that the $LiGa_5O_8:Cr^{3+}$ phosphor is suitable as a stress sensor.

Diffuse reflectance, PL, PLE, and PersL properties of $LiGa_5O_8:Cr^{3+}$

Diffuse reflectance (DR) spectra were used to study the absorption/reflection performance of Cr^{3+}-doped $LiGa_{5(1-x)}O_8:5xCr^{3+}$ (**Figure 3**a). For each Cr^{3+}-doped sample, the DR spectrum shows a plateau for wavelengths above 700 nm and a steep decrease with shoulders from 320 to 230 nm. Absorption near 230 nm is attributed to the host band absorption, and the absorption bands centered at ~290, 420, and 590 nm correspond to the $^4A_2 \rightarrow {}^4T_1$ (^4P), $^4A_2 \rightarrow {}^4T_1$ (^4F), and $^4A_2 \rightarrow {}^4T_2$ (^4F) transitions of Cr^{3+} cations, respectively. These absorption intensities further enhanced on increasing the Cr^{3+} content.[40] To experimentally estimate the bandgap scale, the plot of $[F(R\infty)h\nu]^2$ versus $(h\nu - E_g)$ is shown in Figure 3b. $F(R\infty)$ originates from the Kubelka–Munk function, $F(R\infty) = (1 - R\infty)^2/(2R\infty)$, where $R\infty$ is the reflectivity

value, $h\nu$ is the photon energy, and E_g is the optical bandgap. The spectrum demonstrates a linear dependence of $[F(R\infty)h\nu]^2$ on ($h\nu$ - E_g), indicating that $LiGa_5O_8$ is a direct bandgap material. The optical bandgap of $LiGa_5O_8$ is calculated to be E_g = 4.92 eV from the line extrapolation for $[F(R\infty)h\nu]^2 = 0$ (Figure 3b).[41] Figure 3c-d presents the PL and PLE spectra of $LiGa_{5(1-x)}O_8:5xCr^{3+}$ at room temperature. When the emission was monitored at 716 nm, several broad spectral bands ranging from 240 to 650 nm were observed in the PLE spectra. The band peaking at 246 nm belongs to the host band-to-band absorption, which is in good agreement with Figure 3a.[42] The band peaking at ~290 nm is due to the $^4A_2 \rightarrow {}^4T_1$ (^4P) Cr^{3+} transition. Meanwhile, the two excitation bands centered at 418 and 600 nm, belonging to the $^4A_2 \rightarrow {}^4T_1$ (^4F) and $^4A_2 \rightarrow {}^4T_2$ (^4F) transitions, respectively, resulted from the d–d intrashell transitions of Cr^{3+} ions.[43, 44] We also measured the PL spectra of all Cr^{3+}-doped samples between 650 and 830 nm under 254-nm excitation, and an intense emission band centered at 716 nm was observed. This result corresponds to the spin-forbidden $^2E \rightarrow {}^4A_2$ transition of Cr^{3+} in a 6-fold coordinated site.[45, 46] The Stokes phonon side bands (PSB) were observed at 726 and 738 nm and the anti-Stokes PSB at 702 nm.[47] The inset of Figure 3d shows the deep red image of sample x = 0.12% under a 254-nm lamp. An abnormal PL band is observed in the dotted red rectangle (730–830 nm), which results from the spin-allowed transition between the $^4T_2$ state and the ground state of Cr^{3+}. From the spectral variation shown in Figure 3d, it can be speculated that the increase in the Cr^{3+}-doping concentration is beneficial for enhancing the wide-band emission and inhibiting the 716-nm emission. The persistent luminescence (PersL) spectra were detected and recorded after irradiation with a 254-nm UV lamp for 30 s, as shown in Figure 3e. Moreover, such PersL signals last longer than 10 h (Figure S1). Intriguingly, another broad PersL band in the NIR range extending from 726 to 1000 nm was observed. The PersL peak at 716 nm is attributed to the $^2E \rightarrow {}^4A_2$ transition of Cr^{3+}, while the PersL broad band in the NIR range may originate from the spin-allowed $^4T_2$

$\rightarrow {}^4A_2$ transition, as reported in previous works.[42] To determine the dependence of the PL and PersL intensities at 716 nm and band emission on the Cr^{3+} content, the spectra in Figure 3f, which combine Figure 3d-e, are reported.

When the Cr^{3+} content is increased, the intensity of the 716-nm Cr^{3+} peak first decreased until x = 0.16% and then increased with a further increase in the doping concentration. However, the PersL intensity of the band continuously increases even until x = 0.24%, which indicates that a higher Cr^{3+}-doping concentration will result in enhanced transitions between the ${}^4T_2$ state and the ground state.[43] To further confirm the origin of the 702-, 726-, and 738-nm PL peaks and the broad band PL (740–1000 nm), we measured the PLE and PL decay profile spectra, as reported in Figure S1. From these PLE spectra, we first confirmed that Cr^{3+} is the emitting center. Second, the emission at approximately 800 nm presents a slight red shift (see Figure S2a), which is ascribed to the ${}^4T_2 \rightarrow {}^4A_2$ transition. Meanwhile, both emissions at 702 and 726 nm are attributed to ${}^2E \rightarrow {}^4A_2$ PSB emissions or Cr^{3+}/Cr^{3+} pairs, which affect the crystal field splitting.[48, 49] Furthermore, as expected, the PLE intensity at approximately 800 nm gradually increases with increasing Cr^{3+} content (Figure S2b). Then, a small band shift in the PLE spectra with Cr^{3+} content was observed (Figure S2a-b) with respect to the R line emission at 716 nm. The lifetime values at various wavelengths, including 702, 716, 726, 738, and 800 nm (of the sample containing x = 0.12%), were determined using the following equation:

$$\tau = \frac{\int I(t)tdt}{\int I(t)dt}, \quad (1)$$

where *I(t)* represents the PL intensity at time *t*.[42] Obviously, ${}^2E$ unperturbed emission (716 nm) has the longest lifetime of 2.23 ms. A shorter lifetime (1.80 ms) is obtained for Cr-pairs

(738 nm) than for the 716-nm emission. The shortest lifetime value (0.75 ms) corresponds to the spin-allowed $^4T_2$ emission (800 nm) (Figure S2c-d). Notably, the indicated values correspond to a thermal equilibrium between the ^2E and $^4T_2$ levels, which indicates the intermediate crystal field strength of the Cr^{3+} cations in the $LiGa_5O_8$ host.

Insights on traps responsible for ML

In general, both PersL and ML performances are closely related to traps.[50-53] The TL measurement is extensively used to study the traps, and we also used it for the present work. Because $LiGa_5O_8$:Cr^{3+} does not need post-irradiation stimulation to realize ML, the TL glow curves of $LiGa_{5(1-x)}O_8$:$5xCr^{3+}$ were obtained with different doping concentrations (x = 0, 0.04%, 0.08%, 0.12%, 0.16%, 0.20%, and 0.24%) (**Figure 4**a). However, only negligible TL signals can be recorded in both $LiGa_5O_8$ hosts and various Cr^{3+}-doped samples (Figure 4a), and therefore, it is challenging to study the intensity dependence on traps. It should be noted that blackbody emission is observed at higher temperatures (>500 K), as shown in Figure 4a and 4d. Therefore, we measured the TL glow curves of $LiGa_5O_8$ and Cr^{3+}-doped $LiGa_5O_8$ after UV exposure stimulation (Figure 4b). These curves can be divided into three temperature ranges: ~390 K (P_1), 460 K (P_2), and 530 K (P_3). Based on Urbach's empirical formula[54], the following values were obtained: $E_T = T_m/500 = 23kT_m$, where E_T (eV) is the average trap depth and T_m (K) is the peak temperature in the TL glow curve, which are mainly located at the energy depths of 0.78 eV, 0.92, and 1.06 eV, respectively. The suitable trap depths for PersL are widely recognized as 0.6–0.9 eV;[55,56] the deeper traps at approximately 1.06 eV may play a crucial role in the ML properties of Cr^{3+}-doped $LiGa_5O_8$. Furthermore, with the increase in the Cr^{3+} content, the TL intensities of P_1 and P_2 first decreased to a minimum at x = 0.12%, and then gradually increased. However, P_3 showed a different trend.

A comparison of the TL glow curves of the samples (x = 0.04% and x = 0.12%) before and after UV exposure using the 254-nm lamp (Figure 4c) showed that the x = 0.12% sample has a stronger ML intensity than the x = 0.04% sample, and that the pre-irradiated samples exhibit stronger ML intensity. These results indicate that the traps in P_3 play a more critical role in the ML process. The traps may also be associated with the defects formed during high-temperature sintering in air.[57]

Because traps corresponding to P_3 are the key factors for generating ML, trap regulation and the control of trap distributions by reducing the ratio of $(P_1+P_2)/P_3$ is important for obtaining a stronger ML intensity. Following this idea, we prepared a series of ML phosphors based on the best ML sample $LiGa_{4.994}O_8$:0.6%Cr^{3+} by codoping with Al^{3+} ions in order to vary the trap distribution in $LiGa_{4.994(1-y)}O_8$:0.006Cr^{3+}, 4.994yAl^{3+} (y = 0, 0.02%, 0.04%, 0.06%, 0.08%, and 0.10%). The TL glow curves of Cr^{3+}/Al^{3+}-codoped samples after UV exposure are shown in Figure 4e. With the increase in the Al^{3+} content from y = 0 to 0.10%, the TL intensity of the phosphors first increased to a maximum at y = 0.04% and then decreased with a further increase in the doping concentration. Figure 4f shows the normalization of the TL glow curves by the peak at 390 K, which shows the smallest ratio of $(P_1+P_2)/P_3$ at y = 0.04%. We noticed that the ML intensity of these codoped samples also reached a maximum at y = 0.04% in $LiGa_{4.992}O_8$:0.6%Cr^{3+}, 0.2%Al^{3+} (y = 0.04%) (Figure S3a-b). Single phases of the Al^{3+}-codoped samples were also confirmed, as shown in Figure S3c. Thus, we confirmed that traps located in the P_3 thermal range efficiently contributed to the ML. These traps are important for increasing the deep trap numbers for ML because the shallow traps and medium traps (0.6–0.9 eV) are rapidly emptied owing to the temperature perturbation. In contrast, deep

traps (>0.9 eV) can only be emptied by ML or photo-stimulation with larger energy excitations. Hence, increasing the number of deep traps is a novel way to enhance the ML.

Self-recoverability of ML and mechanism for the ML of $LiGa_5O_8:Cr^{3+}$

Obtaining the ML signal without any UV exposure stimulation is considered to be a self-recoverable feature. We recorded the ML spectra of $LiGa_{4.992}O_8$:0.6%Cr^{3+} and 0.2%Al^{3+} under 10 continuous load cycles, as shown in **Figure 5**. Each load cycle was designed to load 2000 N while holding for 5 s before deloading. ML in this system displays self-recoverability in a dark room after each loading cycle, which also maintains the stable phase, as shown in the XRD pattern after grinding (Figure S4). In addition, such ML self-recoverability is maintained after 0, 10, and 15 days, making $LiGa_{4.992}O_8$:0.6%Cr^{3+}, 0.2%Al^{3+} highly promising as a "stable" stress-sensing material. To further investigate the ML performance of Cr-doped $LiGa_5O_8$, density functional theory (DFT) was used to investigate the electronic structures. For pristine $LiGa_5O_8$, the real spatial 3D orbital contour plot demonstrates that the active bonding and anti-bonding near the Fermi level (E_F) are located near the O and Ga sites, respectively. The lattice displayed a uniform electronic distribution (**Figure 6**a). For the electronic structures, the projected partial density (PDOS) of states is illustrated. Notably, the O-2p orbitals dominate the valence band maximum (VBM), while the s and p orbitals of Ga contribute to the conduction band minimum (CBM). Li showed a highly limited s-orbital contribution (Figure 6b). The introduction of Cr did not significantly affect the lattice structure, which is consistent with the experimental characterizations. However, the introduction of Cr did lead to uneven electronic distributions; as a result, the local piezo-electrical field enhanced the charge separation and recombination. It is noted that the Cr-3d orbitals play a key role in both the anti-bonding and bonding near E_F (Figure 6c). The PDOSs

of Cr-doped $LiGa_5O_8$ further support the significant contribution of Cr in modifying the local electronic structures. Moreover, interelectronic levels are formed by Cr dopants, which facilitate electron transfer to enhance the ML performance (Figure 6d). Further introduction of Al supplies additional traps that facilitate the luminescence by optimizing the trap distributions (Figure S6). To summarize the electron transfer behaviors in Cr-doped $LiGa_5O_8$, we have illustrated the gap states as trap levels to actualize the ML. Formation of interelectronic levels helped alleviate the large barriers for the electronic excitation and transition from the valence band (VB) to the conduction band (CB). The identified trap depths vary from 0.85 to 1.30 eV, which are close to the experimental observations, supporting the enhanced ML performance. Moreover, the electronic levels of the Cr dopant are close to the trap levels, resulting in two possible electron transfer channels to realize ML. The electrons stored in the traps recombine with the holes to supply energy for the excitation of Cr ions for luminescence. Such electrons can also transfer energy to the excitation levels of Cr ions through tunneling because of the close energy levels, which further increases the ML efficiency (Figure 6e). Owing to the noncentrosymmetric structure of the $LiGa_5O_8$ crystal, the introduction of Cr ions further breaks the local symmetry, leading to a stronger local piezoelectric field and ML process. The mechanism can be summarized as follows. (1) Traps are charged by the formation of a piezoelectric field because of the noncentrosymmetric nature of the $LiGa_5O_8$ crystal. (2) Under an external mechanical excitation, electrons are detrapped from the traps to the CB owing to band bending caused by the piezoelectric field. These electrons can also directly tunnel to the dopant levels of Cr. (3) Nonradiative energy is released by electron–hole recombination to excite the Cr ions. (4) The relaxation of excited electrons of Cr ions leads to ML. Therefore, the remarkable ML performance in Cr-doped $LiGa_5O_8$ is attributed to the formation of a local piezoelectric field by the perturbation of the

electronic distribution, induced trap states, and appropriate interelectronic levels, promoting electron transfer and energy conversion.

Potential applications and outlook

Because self-recoverable ML does not require a light-charging process, it can be applied for *in situ* and real-time stress monitoring. Moreover, Cr^{3+}-doped phosphors have been widely reported to have potential applications in bioimaging.[58] Thus, the ML of Cr^{3+}-doped $LiGa_5O_8$ located in the deep-red-to-near-infrared range is promising for biomechanical applications because it is well adapted to the first biological window.[59, 60] As shown in Figure S5a-c, the ML light can be detected even after passing through a 2-mm-thick piece of pork, including the skin, fat, and lean parts (the pork used in this experiment is shown in Figure S5d). These results confirm that Cr^{3+}-doped $LiGa_5O_8$ phosphor can be used for *in situ* and real-time detection of intracorporeal stress/strain and hence can have various bio-applications. More importantly, the self-recoverable ML can reduce the potential irradiation-induced damage to biological tissues because post-stimulation using UV light is not required during the entire operation process. Notably, if we only compared the peak intensity (716 nm) before and after the penetration, the penetration efficiencies (remaining ML intensities) of such NIR ML signals would be retained at a relatively low level (≤10%). We believe that future studies will further improve this efficiency. This preliminary work is a proof-of-concept that NIR ML can be initiated in $LiGa_5O_8$:Cr^{3+} by utilizing the stress load.

Future studies should focus on the following three aspects. i) Although we have presented a way to improve the ML intensity by increasing the proportion of deeper traps through codoping and electronic modulations, this regulation strategy has still very limited

applications. Hence, more advanced and flexible methods for further intensity enhancement are required. ii) Regarding the deep red wavelength of ML peaking at 716 nm, developing new ML phosphors in the first biological window and near-infrared range for deep *in vivo* applications is of great importance. iii) The synthesis and control of nanosized, stable, and dispersible materials to further optimize the properties to an even higher level will be highly significant as well.

Conclusions

This is the first report on the self-recoverable ML behavior in $LiGa_5O_8:Cr^{3+}$, which is located in the deep red wavelength range. In contrast to most ML materials that require stimulation through UV light to power ML emission, the $LiGa_5O_8:Cr^{3+}$ phosphor is triggered solely by mechanical loading. We compared the PersL, TML, ML, and PL performances, and the relationship between the ML intensity and the TL performance. We demonstrated that the deep traps with trap depths of >1.06 eV are responsible for the efficient ML. Consequently, Al^{3+} ions are introduced into the host to regulate the trap distributions and electronic structures to optimize the ML performance. The $LiGa_{4.992}O_8$:0.6%Cr^{3+}, 0.2%Al^{3+} sample showed efficient ML. We have demonstrated that the ML of $LiGa_5O_8:Cr^{3+}$ is self-recoverable without any post-irradiation stimulation after every mechanical loading cycle. A possible mechanism is proposed to elucidate the self-recoverable ML of $LiGa_5O_8:Cr^{3+}$. The DFT calculations confirm that Cr dopants alleviate the electron excitation barriers from CB to VB by forming gap states within the bandgap, which improves the ML through deep electron traps and electronic transfer. The current work not only increases the number of ML candidate materials, but also provides a more comprehensive understanding of the ML mechanism. Finally, we have demonstrated that such ML light can penetrate 2-mm-thick pork with skin,

fat, and lean parts, indicating that the $LiGa_5O_8:Cr^{3+}$ phosphor can be useful for *in vivo* bioimaging applications.

Experimental Section

Synthesis of $LiGa_5O_8:Cr^{3+}$ and $LiGa_{5-x}Al_x\ O_8:Cr^{3+}$ powders. All $LiGa_5O_8:Cr^{3+}$ and $LiGa_5O_8:Cr^{3+}$, Al^{3+} (or $LiGa_{5-x}Al_x\ O_8:Cr^{3+}$) powders were synthesized by a high-temperature solid-state reaction.[61] High-purity Li_2CO_3 (99.99%, Aladdin, lot#L101684), Ga_2O_3 (99.99%, Aladdin, lot#1921038), Al_2O_3 (99.99%, Aladdin, lot#E1831157), and Cr_2O_3 (99.99%, Aladdin, lot#L1305023) were weighed according to the chemical composition. $LiGa_{5(1-x)}O_8:5xCr^{3+}$ (x = 0.04%, 0.08%, 0.12%, 0.16%, 0.20%, and 0.24%) and $LiGa_{4.994(1-y)}O_8:0.6\%Cr^{3+}$, $4.994yAl^{3+}$ (y = 0, 0.02%, 0.04%, 0.06%, 0.08%, and 0.10%) powders were ground in an agate mortar. Then, the samples were sintered with an air flow initially at 800 °C for 2 h and then at 1400 °C for 4 h. After sintering, the samples were slowly cooled down to room temperature in the furnace and ground again for subsequent characterization.

Characterizations. The crystalline phases of $LiGa_{5(1-x)}O_8:5xCr^{3+}$ (x = 0.04%, 0.08%, 0.12%, 0.16%, 0.20%, and 0.24%) and $LiGa_{4.994(1-y)}O_8:0.6\%Cr^{3+}$, $4.994yAl^{3+}$ (y = 0, 0.02%, 0.04%, 0.06%, 0.08%, and 0.10%) were characterized using an X-ray diffractometer (Rigaku D/max-IIIA) with Cu-Kα1 radiation (1.5405 Å; cathode voltage, 40 kV; current, 40 mA) as the X-ray radiation source and swept in the 2θ range of 10°–90° at room temperature. Raw XRD data were further analyzed using the Rietveld refinement method (FullProf software package) to confirm the formation of the target phase, and the crystal structure of $LiGa_5O_8$ was redrawn according to $LiGa_5O_8$ PDF number 38-1371. To confirm the stability of the sample during ML-loading cycles, we ground the sample with optical epoxy resin into powder for the XRD

test before and after the grinding test. Diffuse reflectance (DR) spectra were obtained with an Agilent Cary 60 ultraviolet-visible spectrometer over the range of 200−1000 nm using $BaSO_4$ powder as a standard reference. Morphological and elemental analyses were performed using a Hitachi S-3700 scanning electron microscope equipped with an energy-dispersive X-ray spectrometer at a working voltage of 15.0 kV. Static photoluminescence excitation (PLE), emission (PL) (slits: 1.4, 1.4), and dynamic persistent luminescence (PersL) (slits: 5, 5) spectra were recorded using an Edinburgh FLS920 fluorescence spectrometer equipped with a 450-W Xe lamp source. For thermoluminescence (TL) measurements, the samples were pre-irradiated with a 15-W, 254-nm lamp. The TL glow curves were recorded using an FJ427A1 thermoluminescent dosimeter (CNNC Beijing Nuclear Instruments Factory) in the range of 320–620 K at a heating rate of 2 K/s. To evaluate the ML properties of the samples, composite pellets (diameter: 25 mm; thickness: ~5 mm) were prepared by mixing the ML powders with an optical epoxy resin (ZM DIY) at a mass ratio of 1:4. The epoxy resin and the powders were mixed by magnetic stirring for 20 min to improve the dispersion homogeneity of the powders. The ML spectra and static PersL spectra (Figure 3e) were recorded using a photon-recording system consisting of a fiber optical spectrometer (QE65pro, Guangzhou BiaoQi Optoelectronics) and a computer. Before the ML test, the pellets were stored in a dark room for 12 h to exclude possible UV exposure. For one loading cycle, the load rate was 100 mm/min, the integration time of QE65pro was 800 ms, and the detector was a 1.2-m long fiber with a numerical aperture of 0.22 and a diameter of 600 μm. Compression was used to generate ML for loading cycles in a dark room, and no UV exposure was used during the ML measurements. All images were recorded using a Canon EOS 700D digital camera (ISO: 3200, AV mode, EFS 18-55 mm).

Calculation Setup. All calculations were carried out using density functional theory (DFT) within the CASTEP package regarding the electronic structures and energy cost of doping.[62, 63] For all calculations, we chose the generalized gradient approximation (GGA) and Perdew-Burke-Ernzerhof (PBE) to reveal the exchange-correlation energy.[64-66] We selected the 410-eV cut-off energy within the ultrasoft pseudopotential scheme for all geometry optimizations.[67] The Broyden–Fletcher–Goldfarb–Shannon (BFGS) algorithm was applied to the k-point mesh to achieve energy minimizations.[68,69] For all geometry optimizations, we set the convergence criteria for the geometry optimizations as follows: the Hellmann-Feynman forces should not exceed 0.001 eV per angstrom, and the total energy should be less than 5×10^{-5} eV per atom. For doping, the Cr atom was placed in the position of the Ga site to align with the experimental observations, and the doping concentration was 5% for all the theoretical calculations.

Supporting Information

Supporting Information is available from the Wiley Online Library or from the author.

Acknowledgements

We acknowledge financial support from the National Natural Science Foundation of China (Grant No. 51672085, 51872095, 21771156), Program for Innovative Research Team in University of Ministry of Education of China (Grant No. IRT_17R38), Major Basic Research Cultivation Project of Natural Science Foundation of Guangdong Province (Grant No.2018B03038009), Local Innovative Research Team Project of "Pearl River Talent Plan" (Grant No. 2017BT01X137), and the Early Career Scheme (ECS) fund (Grant No.: PolyU 253026/16P) from the Research Grant Council (RGC) in Hong Kong. P. X. Xiong thanks Z.Q. Huang for his help with the SEM test, B.B. Su for help with the XRD test, and R.H. Ma for his help with the ML test.

Received: ((will be filled in by the editorial staff))
Revised: ((will be filled in by the editorial staff))
Published online: ((will be filled in by the editorial staff))

References

[1]. R. R. Petit, S. E. Michels, A. Feng and P. F. Smet, Light Sci Appl 8 (2019) 1-10.

[2]. X. Wang, D. Peng, B. Huang, C. Pan and Z. L. Wang, Nano Energy 55 (2019) 389-400.

[3]. J.-C. Zhang, X. Wang, G. Marriott and C.-N. Xu, Pro Mater Sci 103 (2019) 678-742.

[4]. C. Chen, Y. Zhuang, D. Tu, X. Wang, C. Pan and R.-J. Xie, Nano Energy 68 (2020) 104329.

[5]. Feng, S. Michels, A. Lamberti, W. Van Paepegem and P. F. Smet, Acta Mater 183 (2020) 493-503.

[6]. F. Wang, F. Wang, X. Wang, S. Wang, J. Jiang, Q. Liu, X. Hao, L. Han, J. Wang, C. Pan, H. Liu and Y. Sang, Nano Energy 63 (2019) 103861.

[7]. L. Liu, C.-N. Xu, A. Yoshida, D. Tu, N. Ueno and S. Kainuma, Adv Mater Tech 4, (2019) 1800336.

[8]. M. C. Wong, L. Chen, G. Bai, L. B. Huang and J. Hao, Adv Mater 29 (2017) 129.

[9]. X. Y. Wei, X. Wang, S. Y. Kuang, L. Su, H. Y. Li, Y. Wang, C. Pan, Z. L. Wang and G. Zhu, Adv mater 28 (2016) 6656.

[10]. X. Wang, H. Zhang, R. Yu, L. Dong, D. Peng, A. Zhang, Y. Zhang, H. Liu, C. Pan and Z. L. Wang, Adv mater 27 (2015) 2324.

[11]. W. Li, Q. Huang, Z. Mao, Q. Li, L. Jiang, Z. Xie, R. Xu, Z. Yang, J. Zhao, T. Yu, Y. Zhang, M. P. Aldred and Z. Chi, Angew Chem Int Ed 57 (2018) 12727-12732.

[12]. R. S. Fontenot, K. N. Bhat, W. A. Hollerman and M. D. Aggarwal, Materials Today 14 (2011) 292-293.

[13]. A. Incel, M. Emirdag-Eanes, C. D. McMillen and M. M. Demir, ACS Appl Mater Interfaces 9 (2017) 6488-6496.

[14]. Xie, Y. and Z. Li. Chem 4 (2018) 943-971.

[15]. S.M. Jeong, S. Song, S-K. Lee and B. Choi, Appl Phys Lett 102 (2013) 051110.

[16]. Q. Hua, J. Sun, H. Liu, R. Bao, R. Yu, J. Zhai, C. Pan and Z. L. Wang, Nat Commun 9 (2018) 244.

[17]. L. Li, L. Wondraczek, M. Peng, Z. Ma and B. Zou, Nano Energy 69 (2020) 104413.

[18]. X. Zhang, J. Zhao, B. Chen, T. Sun, R. Ma, Y. Wang, H. Zhu, D. Peng and F. Wang, Adv Opt Mater 8, (2020) 2000274.

[19]. D. Peng, Y. Jiang, B. Huang, Y. Du, J. Zhao, X. Zhang, R. Ma, S. Golovynskyi, B. Chen and F. Wang, Adv Mater 32 (2020) 1907747.

[20]. P. Xiong and M. Peng, J Mater Chem C 7 (2019) 6301-6307.

[21]. H. Zhang, D. Peng, W. Wang, L. Dong and C. Pan, The J Phy Chem C 119 (2015) 28136-28142.

[22]. H. Li, Y. Zhang, H. Dai, W. Tong, Y. Zhou, J. Zhao and Q. An, Nanoscale 10 (2018) 5489-5495.

[23]. P. Xiong, M. Peng, J. Cao and X. Li, J Am Cera Soc 102 (2019) 5899-5909.

[24]. C. Wang, D. Peng and C. Pan, Sci Bull 65 (2020) 1147-1149.

[25]. B. Huang, Phys Chem Chem Phys 18 (2016) 25946-25974.

[26]. B. Huang, M.Z. Sun and D.F. Peng, Nano Energy 47 (2018) 150-171.

[27]. S. M. Jeong, S. Song, S. K. Lee and N. Y. Ha, Adv mater 25 (2013) 6194.

[28]. K.-S. Sohn, S. Timilsina, S. P. Singh, T. Choi and J. S. Kim, APL Mater 4 (2016) 106102.

[29]. J. Botterman, K. V. d. Eeckhout, I. D. Baere, D. Poelman and P. F. Smet, Acta Mater 60 (2012) 5494-5500.

[30]. Y. Du, Y. Jiang, T. Sun, J. Zhao, B. Huang, D. Peng and F. Wang, Adv Mater 31 (2018) 1807062.

[31]. D. Tu, C. N. Xu, A. Yoshida, M. Fujihala, J. Hirotsu and X. G. Zheng, Adv Mater 29 (2017) 129.

[32]. W. Wang, D. Peng, H. Zhang, X. Yang and C. Pan, Opt Commun 395 (2017) 24.

[33]. S.K. Sharma, D. Gourier, B. Viana, T. Maldiney, E. Teston, D. Scherman, C. Richard, Opt Mater 36 (2014) 1901-1906.

[34]. A. Bessière, A. Lecointre, R.A. Benhamou, E. Suard, G. Wallez, B. Viana, J Mater Chem C 1 (2013) 1252-1259.

[35]. H. Chen, X. Sun, G. D. Wang, K. Nagata, Z. Hao, A. Wang, Z. Li, J. Xie and B. Shen, Mater Hori 4 (2017) 1092-1101.

[36]. F. Liu, W. Yan, Y. J. Chuang, Z. Zhen, J. Xie and Z. Pan, Sci Rep 3 (2013) 1554.

[37]. P.J. Dereń, M. Malinowski, W. Stręk, J Lumin 68 (1996) 91-103.

[38]. J. L. Goldman, B. R. Long, A. A. Gewirth and R. G. Nuzzo, Adv Funct Mater 21 (2011) 2412-2422.

[39]. H. X. Zhao, C. X. Yang and X. P. Yan, Nanoscale 8 (2016) 18987.

[40]. X. Lin, R. Zhang, X. Tian, Y. Li, B. Du, J. Nie, Z. Li, L. Chen, J. Ren, J. Qiu and Y. Hu, Adv Opt Mater 6 (2018) 1701161.

[41]. H. Li, R. Pang, G. Liu, W. Sun, D. Li, L. Jiang, S. Zhang, C. Li, J. Feng and H. Zhang, Inorg Chem 57 (2018) 12303-12311.

[42]. Q. De Clercq and D. Poelman, ECS J Solid State Sci. Technol. 7 (2018) 3171-3175.

[43]. Q. De Clercq, J. Du, P. F. Smet, J. J. Joos and D. Poelman, Phys Chem Chem Phys 20 (2018) 30455-30465.

[44]. A. Viana, S. K. Sharma, D. Gourier, T. Maldiney, E. Teston, D. Scherman and C. Richard, J Lumin 170 (2016) 879-887.

[45]. G. Liu, S. Zhang, Y. Shi, X. Huang, Y. Tang, P. Chen, W. Si, W. Huang and X. Dong, Adv Funct Mater 28 (2018) 1804317.

[46]. W. Fan, N. Lu, C. Xu, Y. Liu, J. Lin, S. Wang, Z. Shen, Z. Yang, J. Qu, T. Wang, S. Chen, P. Huang and X. Chen, ACS Nano, 11 (2017) 5864-5872.

[47]. Gourier, A. Bessière, S. K. Sharma, L. Binet, B. Viana, N. Basavaraju and K. R. Priolkar, Phy and Chem Sol 75 (2014) 826-837.

[48]. H. Lin, G. Bai, T. Yu, M.-K. Tsang, Q. Zhang and J. Hao, Adv Opt Mater 5 (2017) 1700227.

[49]. V. Đorđević, M. G. Brik, A. M. Srivastava, M. Medić, P. Vulić, E. Glais, B. Viana and M. D. Dramićanin, Opt Mater 74 (2017) 46-51.

[50]. P. Xiong and M. Peng, J Mater Chem C 7 (2019) 8303-8309.

[51]. Z. Pan, Y. Y. Lu and F. Liu, Nat Mater 11 (2011) 58-63.

[52]. P. Xiong and M. Peng, Opt Mater: X 2 (2019) 100022.

[53]. S. K. Sharma, D. Gourier, B. Viana, T. Maldiney, E. Teston, D. Scherman and C. Richard, Opt Mater 36 (2014) 1901-1906.

[54]. A. J. J. Bos, R. M. van Duijvenvoorde, E. van der Kolk, W. Drozdowski and P. Dorenbos, J Lumin 131 (2011) 1465-1471.

[55]. Y. Zhuang, L. Wang, Y. Lv, T.-L. Zhou and R.-J. Xie, Adv Funct Mater 28 (2018) 1705769.

[56]. J. Xu, D. Murata, J. Ueda, B. Viana and S. Tanabe, Inorg Chem 57 (2018) 5194-5203.

[57]. Finley and J. Brgoch, J Mater Chem C 7 (2019) 2005-2013.

[58]. Y. Li, M. Gecevicius and J. Qiu, Chem Soc Rev 45 (2016) 2090-2136.

[59]. P. Xiong, M.Y. Peng and Z.M. Yang, iScience 24 (2021) 101944.

[60]. L.J. Li, L. Wondraczek, L.H. Li, Y. Zhang, Y. Zhu, M.Y. Peng and C.B. Mao, ACS Appl Mater & Interfaces 10 (2018) 14509-14516.

[61]. P. Xiong, M. Peng, K. Qin, F. Xu and X. Xu, Adv Opt Mater 7 (2019) 1901107.

[62]. S. J. Clark, M. D. Segall, C. J. Pickard, P. J. Hasnip, M. J. Probert, K. Refson and M. C. Payne, Zeitschrift Fur Kristallographie 220 (2005) 567-570.

[63]. S. J. Clark, M. D. Segall, C. J. Pickard, P. J. Hasnip, M. I. J. Probert, K. Refson and M. C. Payne, Z Kristallogr Cryst Mater 220 (2005) 1220.

[64]. J. P. Perdew, K. Burke and M. Ernzerhof, Phys Rev Lett 77 (1996) 3865-3868.

[65]. P. J. Hasnip and C. J. Pickard, Comput. Phys Commun 174 (2006) 24-29.

[66]. J. P. Perdew, J. A. Chevary, S. H. Vosko, K. A. Jackson, M. R. Pederson, D. J. Singh and C. Fiolhais, Physical Review B 46 (1992) 6671-6687.

[67]. Vanderbilt, Physical Review B 41 (1990) 7892-7895.

[68]. J. D. Head and M. C. Zerner, Chem Phys Lett 122 (1985) 264-270.

[69]. M. I. J. Probert and M. C. Payne, Phys Rev B 67 (2003) 167.

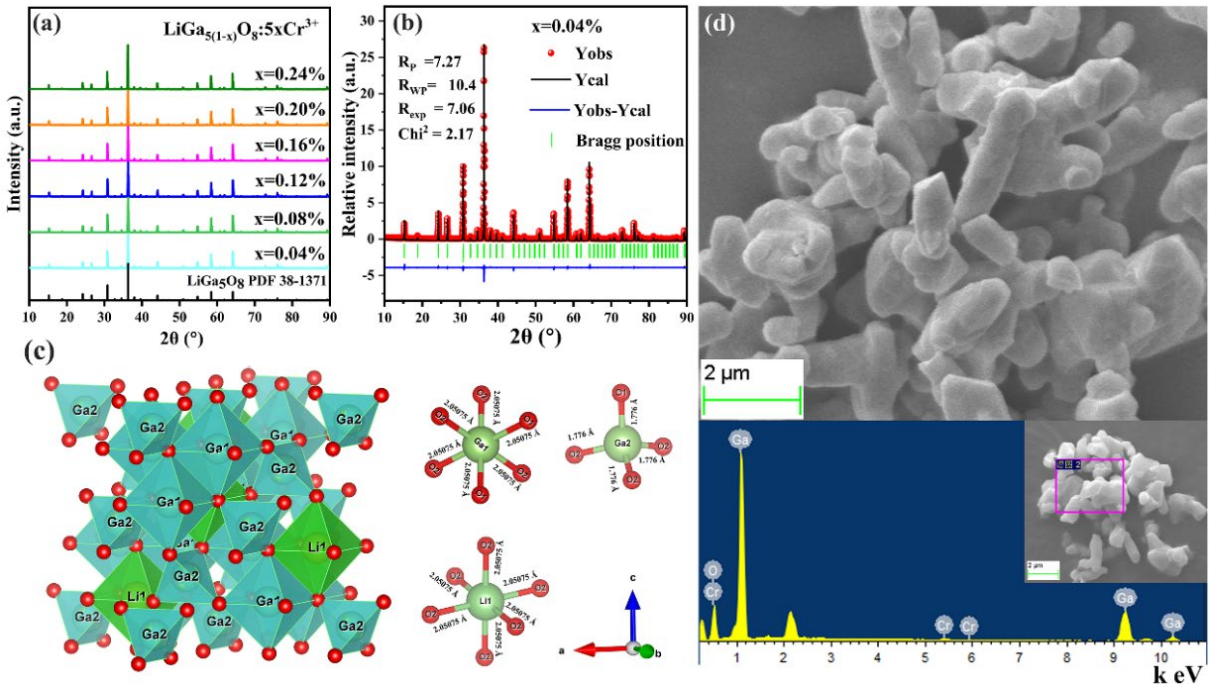

Figure 1 Crystalline structure and micromorphology of $LiGa_5O_8:Cr^{3+}$. (a) XRD patterns of $LiGa_{5(1-x)}O_8:5xCr^{3+}$ (x= 0.04%, 0.08%, 0.12%, 0.16%, 0.20% and 0.24%) and standard card of $LiGa_5O_8$ (PDF 38-1371). (b) XRD pattern (red ○, Y_{obs}) of the sample x=0.04%, Rietveld refining results (black−, Y_{cal}), Bragg reflections (green |, Bragg position) and the profile difference between experimental and calculated values (blue−, Y_{obs}-Y_{cal}). (c) Scheme for the crystalline structure of $LiGa_5O_8$ redrawn on the basis of PDF 38-1171 using VESTA program. (d) SEM image (upside) and EDS pattern (downside, the unlabeled peaks are from Au element brought by the sputtering process before the test) of sample x=0.04%.

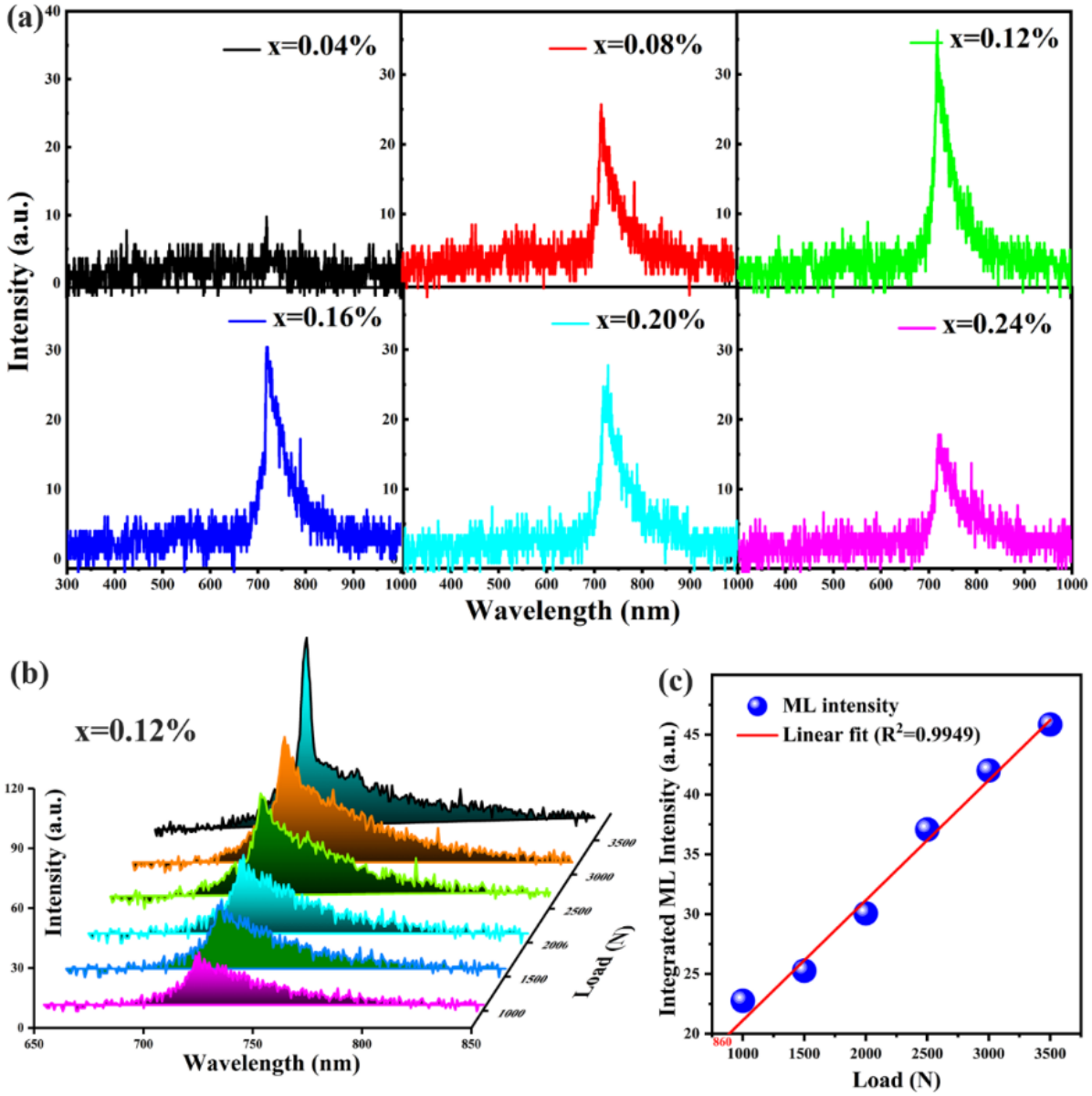

Figure 2 ML features of $LiGa_{5(1-x)}O_8:5xCr^{3+}$. (a) ML spectra of $LiGa_{5(1-x)}O_8:5xCr^{3+}$ as a function of Cr^{3+} content (x=0.04%, 0.08%, 0.12%, 0.16%, 0.20% and 0.24%) under 1000 N load. (b) ML spectra of sample x=0.12% as a function of load (1000, 1500, 2000, 2500, 3000 and 3500 N). (c) Integrated ML intensity for spectra presented in (b). Notice that intercept is 860 N. Integrating range: 600-1000 nm.

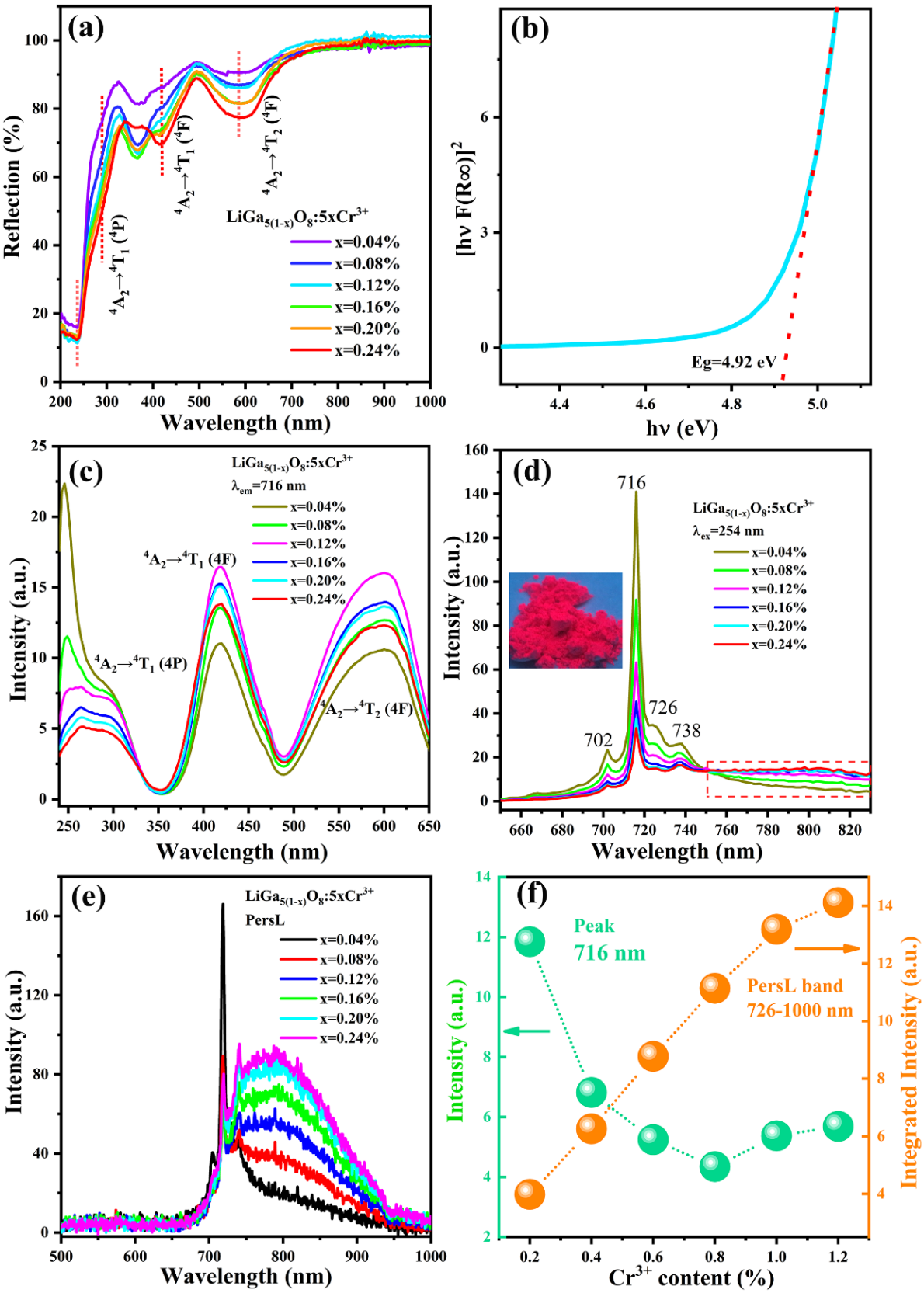

Figure 3 Optical characteristics of $LiGa_{5(1-x)}O_8:5xCr^{3+}$. (a) DR spectra. (b) The plot of $[F(R\infty)h\nu]^2$ versus energy (eV). (c) PLE (λ_{em}=716 nm) and (d) PL (λ_{ex}=254 nm) spectra. The inset of (d) is the image of sample x=0.12% under a 254 nm lamp. (e) PersL spectra recorded

after irradiated by a 254 nm lamp for 30 s. (f) The peak PersL intensities of 716 nm and the PersL band (726-1000 nm) as a function of Cr^{3+} content. The composites are $LiGa_{5(1-x)}O_8:5xCr^{3+}$ (x=0.04%, 0.08%, 0.12%, 0.16%, 0.20% and 0.24%).

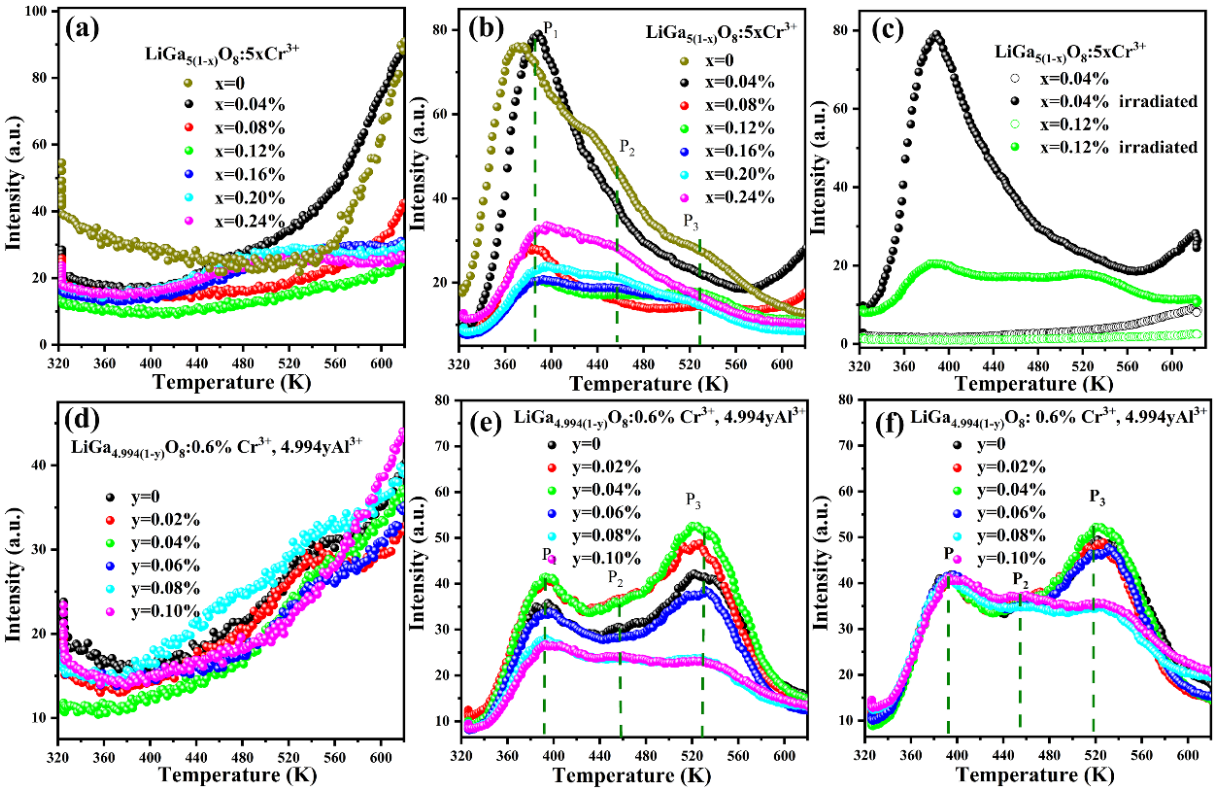

Figure 4 Thermoluminescence glow curves and blackbody emission characteristics. (a) and (d) show the blackbody emissions of $LiGa_{5(1-x)}O_8:5xCr^{3+}$ and $LiGa_{4.994(1-y)}O_8:0.6\%Cr^{3+}$, $4.994yAl^{3+}$, respectively. (b) TL glow curves of $LiGa_{5(1-x)}O_8:5xCr^{3+}$ (x=0, 0.04%, 0.08%, 0.12%, 0.16%, 0.20% and 0.24%) over 320-620 K pre-irradiated by a 254 nm lamp for 30 s. (c) TL glow curves of samples x=0.04% and 0.12% before and after irradiated by a 254 nm lamp for 30 s. (e) TL glow curves of $LiGa_{4.994(1-y)}O_8:0.6\%Cr^{3+}$, $4.994yAl^{3+}$ (y= 0, 0.02%, 0.04%, 0.06%, 0.08% and 0.10%) over 320-620 K pre-irradiated by a 254 nm lamp for 30 s. (f) Normalized TL glow curves of (e) by the TL peak intensity at 390 K.

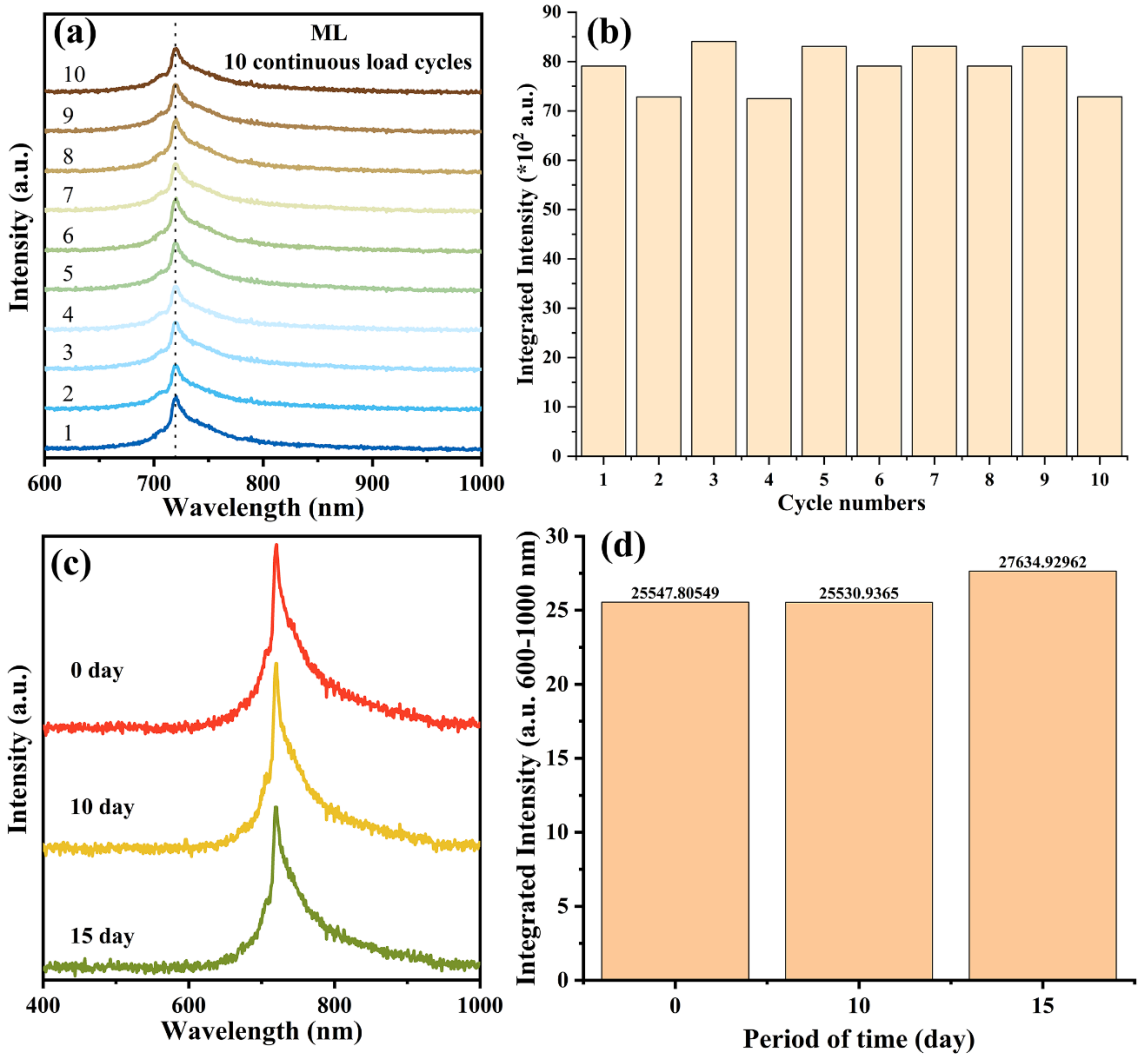

Figure 5 (a) Self-recoverable ML spectra of $LiGa_{4.992}O_8$:0.6%Cr^{3+}, 0.2%Al^{3+}. Load: 2000 N, holding time 5 s. (b) Integrated ML intensities over 600-1000 nm. (c) ML spectra and (d) corresponding integrated ML intensities over 600-1000 nm after 0, 10 and 15 days.

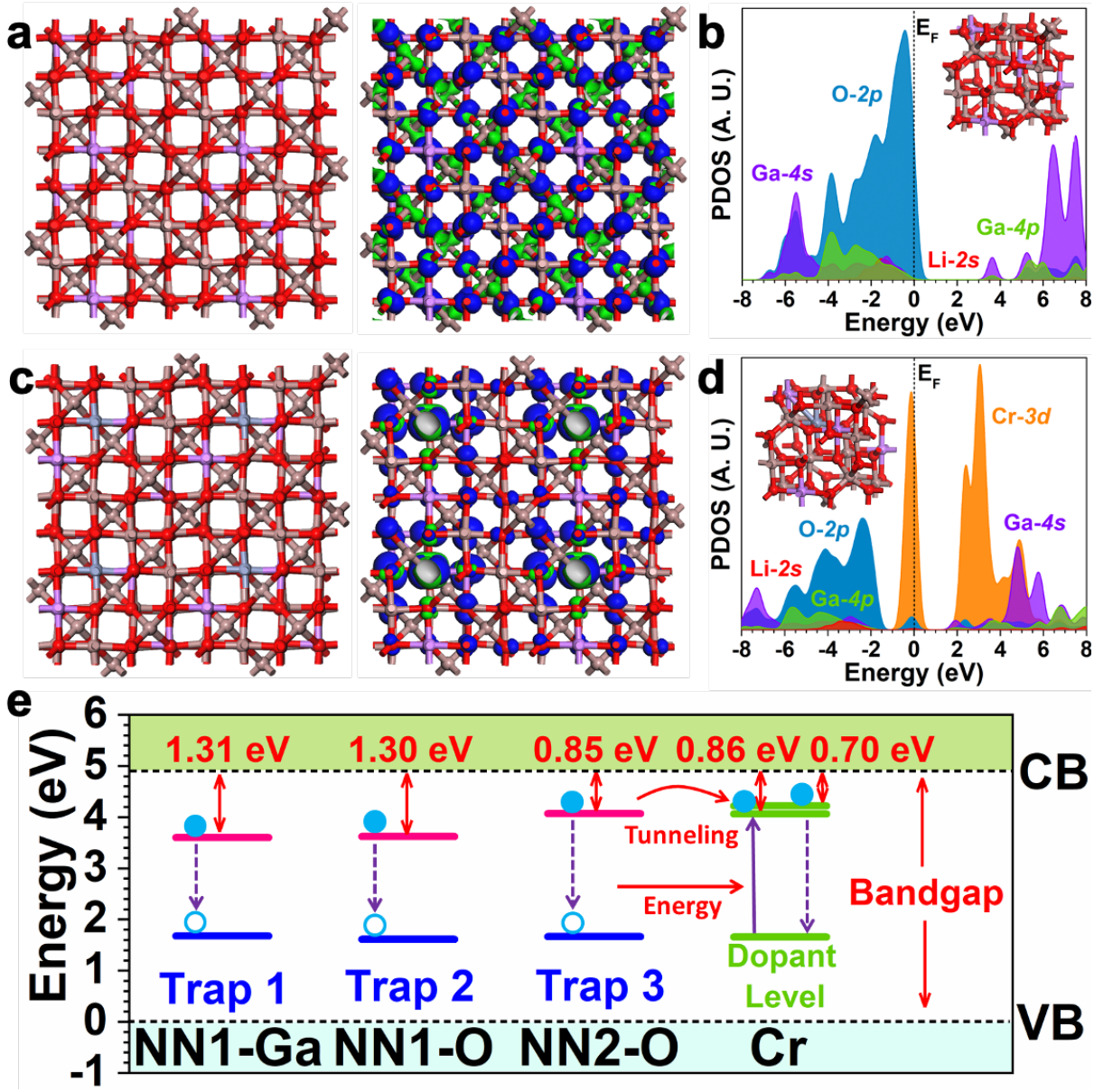

Figure 6 (a) The lattice structure and real spatial 3D orbital contour plots for $LiGa_5O_8$. Purple balls= Li; Brown balls= Ga and Red balls= O. (b) The PDOSs of $LiGa_5O_8$. Inset: lattice structure of $LiGa_5O_8$. (c) The lattice structure and real spatial 3D orbital contour plots for Cr-doped $LiGa_5O_8$. Purple balls= Li; Brown balls= Ga; Red balls= O and Grey balls= Cr. (d) The PDOSs of Cr-doped $LiGa_5O_8$. Inset: lattice structure of Cr-doped $LiGa_5O_8$. (e) The summarized trap levels and electron transfer pathways for Cr-doped $LiGa_5O_8$.

Self-recoverable mechanoluminescence (ML) in Cr^{3+}-doped $LiGa_5O_8$, which overcomes the dependence on UV exposure stimulation, is shown. This ML phosphor realizes a fully reversible ML intensity, which relies on the electronic levels and shallow electron trap distributions. This work provides a novel ML material system for future development in broad bioapplications.

Keyword Mechanoluminescence

P. Xiong, B. Huang*, D. Peng, B. Viana, M. Peng* and Z. Ma*

Self-recoverable mechanically induced instant luminescence from Cr^{3+}-doped $LiGa_5O_8$